International Journal of Thermal Sciences 215 (2025) 110000

Contents lists available at ScienceDirect

International Journal of Thermal Sciences

journal homepage: www.elsevier.com/locate/ijts

Enhanced heat transfer study of solid lithium target for BNCT based on Gyroid structure function regulation

Kaiwen Qin [a,b], Nailiang Zhuang [a,b], Chong Shao [c], Hangbin Zhao [b,c], Xiaobin Tang [a,b,*]

[a] Department of Nuclear Science and Technology, Nanjing University of Aeronautics and Astronautics, Nanjing, 211106, China
[b] Key Laboratory of Advanced Nuclear Technology and Radiation Protection, Ministry of Industry and Information Technology, Nanjing, 211106, China
[c] College of Astronautics, Nanjing University of Aeronautics and Astronautics, Nanjing, 211106, China

ARTICLE INFO

Keywords:
Neutron target station
Gyroid structure
"Through-holes" factor α
Performance evaluation criterion (*PEC*)

ABSTRACT

Accelerator-driven neutron target stations generate a considerable amount of deposited heat that requiring timely and efficient removal to maintain safe operation. In this study, a Gyroid structure substrate was proposed to improve the heat removal capability of the BNCT neutron target stations, and the "through-hole" factor (α) was introduced to optimize the standard Gyroid structure, aiming to enhance its convective heat transfer performance. The flow and heat transfer characteristics of the improved Gyroid structure was analyzed using numerical simulations and experimental measurements. The results show that as the value of α increases, Gyroid structure peak temperature (T_{max}) decreases by 4.9–7.4 K, the convective heat transfer coefficient (h) increases by 4.3 %–8.2 %, and the Nusselt number (Nu) increases by 0.7 %–3.5 %. Taking the comprehensive performance evaluation criterion (*PEC*) as the evaluation index, it is recommended to select $\alpha = 2.0$ to achieve optimal results. This study provides the theoretical support and technical guidance for the design and development of new neutron target stations.

Nomenclature

D_h	Hydraulic diameter (m)	*Greek symbols*	
v	Average of velocity fluid ($m \cdot s^{-1}$)	ρ	Fluid density ($kg \cdot m^{-3}$)
V_f	Volume of TPMS structure fluid region (m^3)	μ	Dynamic viscosity (Pa·s)
A_f	Wetted surface area of TPMS structure (m^2)	λ	Thermal conductivity of fluid ($W \cdot m^{-1} \cdot K^{-1}$)
h	Convective heat transfer coefficient ($W \cdot m^{-2} \cdot K^{-1}$)	*Subscripts*	
Q	Average heat flux density ($W \cdot m^{-2}$)		
T_w	Average temperature of heating surface (K)	w	Wall
T_f	Average temperature of fluid (K)	f	Fluid
T_{in}	Fluid temperature at the inlet (K)	in	Inlet
T_{out}	Fluid temperature at the outlet (K)	out	Outlet
q	Volumetric flow rate ($m^3 \cdot h^{-1}$)	*Dimensionless parameters*	
L	The length of TPMS structural unit (m)		
z	Wall thickness of TPMS structure (m)	Re	Reynolds Number
C	The offset of unit surface	Nu	Nusselt number
Δp	The pressure drop of the fluid through the Gyroid structure	f	Friction factor
		PEC	Performance evaluation coefficient

1. Introduction

The principle of boron neutron capture therapy (BNCT) is to utilize ^{10}B to capture low-energy neutrons, releasing high linear energy α particles and ^{7}Li recoil nuclei within tumor cells, thereby killing the tumor cells [1–4]. Specifically, the accelerator-based neutron source based on the $^{7}Li(p,n)^{7}Be$ reaction has the advantages of a low reaction threshold, average neutron energy, high neutron yield, and easy moderation [5]. Thus, it is ideal for realizing an accelerator neutron source for BNCT [6,7]. However, in the process of neutron production by proton bombardment of the Li target, more than 99.9 % of the energy is deposited in the form of heat in neutron target stations [8]. The melting point of the solid Li target is relatively low (only 453 K), and the export of heat deposited by the high-energy proton beam bombarding the Li target is a very tricky technical problem [9,10]. In particular, the requirement for neutron yield from Li targets increases with the increasing clinical demand for BNCT [11]. Current research approaches have focused on increasing the proton energy or beam intensity to

* Corresponding author. Department of Nuclear Science and Technology, Nanjing University of Aeronautics and Astronautics, Nanjing, 211106, China.
E-mail address: tangxiaobin@nuaa.edu.cn (X. Tang).

https://doi.org/10.1016/j.ijthermalsci.2025.110000
Received 25 December 2024; Received in revised form 10 April 2025; Accepted 10 May 2025
Available online 17 May 2025

improve the neutron yield. However, increasing the proton energy or beam intensity exacerbates the problem of energy deposition [12,13]. Therefore, enhancing the heat removal capability of neutron target stations is a critical challenge in accelerator-driven BNCT neutron source technology.

Various studies on improving the heat removal capabilities of neutron target stations have been conducted globally. Yoshihashi et al. [10] proposed the incorporation of V-shaped staggered ribs into a smooth channel structure to enhance the heat dissipation performance of a neutron target station. The results indicate that using V-shaped staggered ribs can increase the heat transfer coefficient by 2.4 times. Ludewigt et al. [14] designed a V-shaped target consisting of two planar targets, each positioned at an angle of 30° to the proton beam, effectively reducing the thermal load on each target by half. Nakamura et al. [15] designed a multilayered conical target with a 60° apex angle to enhance the heat dissipation by expanding the beam spot area. The rotational method is also effective for the heat dissipation of neutron target stations. Hu et al. [16] designed a rotatable planar neutron target, which under the incidence of a 2.8 MeV, 30 mA proton beam, resulted in a maximum lithium layer temperature of only 83 °C. Wang et al. [17] designed a half-tire-shaped curved lithium target that rotated around its center. For a 50 kW proton beam, the maximum temperature of the curved Li target reaches only 100 °C, effectively meeting its heat dissipation requirements. Current designs for accelerator-driven neutron target stations enhance heat transfer by increasing the heat transfer area, adding ribs and fins to cooling channels, and using other traditional methods. However, the effects of conventional enhanced heat transfer approaches are limited under high proton beam fluxes.

Recently, a type of structure known as a triply periodic minimal surface (TPMS) has attracted considerable attention owing to its compact structural design and excellent thermophysical properties [18–20]. TPMS has numerous advantages, such as porosity, smoothness, connectivity, diversity, and controllability [21–23], which provide new ideas for enhancing heat transfer in single-phase fluids. Various studies have analyzed the heat transfer performance of different TPMS structures. Khalil et al. [24] investigated forced convection in three TPMS-based heat sinks and found that the Gyroid-solid had the lowest friction factor, the Gyroid-sheet had the highest heat transfer coefficient, and the Diamond-solid demonstrated the highest thermal efficiency. Dixit et al. [25] fabricated a gyroid lattice liquid–liquid compact heat exchanger, achieving a 55 % increase in effectiveness compared with a counter-flow heat exchanger. Li et al. [26] showed that Gyroid and Diamond heat exchangers exhibited a 15–100 % improvement in thermal performance over printed circuit heat exchangers (PCHE). Wang et al. [27] studied heat transfer in channels based on various TPMS structures, highlighting the role of secondary flows and directional changes. Empirical correlations were developed for the Nusselt number and friction factor in the turbulent regime.

Numerous studies have demonstrated that TPMS structures have significant advantages in enhancing heat transfer. However, the existing TPMS structural designs have certain limitations. Tang et al. [28] studied the convective heat transfer for three types of TPMS structures (Gyroid, Diamond, and Iwp) by combining numerical simulations and experiments. The study found that Gyroid and Iwp structures exhibit “through-hole” features in the planar view (as shown in Fig. 1). When these “through-holes” exist in the structure, the fluid tends to flow through them owing to the lower flow resistance. This reduces heat transfer between the solid surface and the fluid is disadvantageous for convective heat transfer. Thus, if the “through-holes” in the TPMS structures can be closed, convective heat transfer can be enhanced.

Therefore, this study envisioned that the TPMS function equation could be precisely controlled to gradually close “through-holes” in the TPMS structure. Theoretically, the fluid mixing can be enhanced to improve convective heat transfer based on a standard TPMS structure. Therefore, this study proposes a function regulation method to precisely control the Gyroid structure, which enables the “through-holes” in the Gyroid structure to gradually close. Additionally, the flow and heat transfer characteristics of the improved Gyroid-type TPMS structure were studied using numerical simulation and experimental measurement, and the functional relationships of the Nusselt number, convective heat transfer coefficient, pressure drop, and friction factor with the Reynolds number were analyzed. Therefore, this study provides the theoretical support and technical guidance for the design and development of new neutron targets.

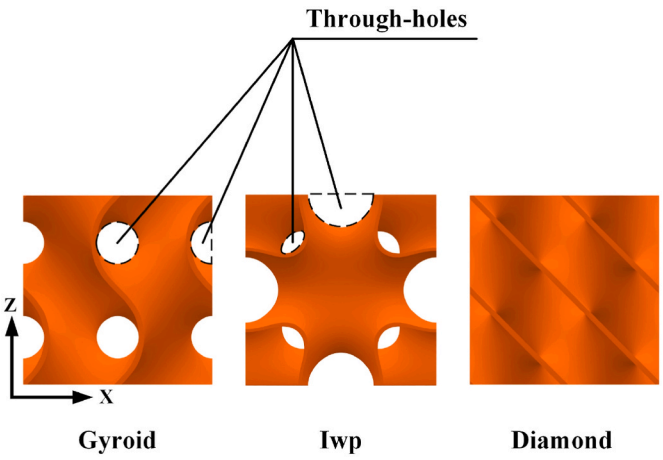

Fig. 1. Plane view of gyroid, diamond and Iwp structure.

2. Neutron target station and improved Gyroid structure

2.1. Neutron target station with Gyroid structure

To enhance the heat removal capability of BNCT neutron targets, a BNCT neutron target design based on a Gyroid structure was proposed in this study, as shown in Fig. 2. The cooling channel inside the neutron target station has dimensions of 120 mm × 120 mm × 10 mm, with a Gyroid structure integrated within the cooling channel to enhance heat transfer (Gyroid structure unit length $L = 10$ mm, thickness $z = 0.5$ mm, and unit surface offset $C = 0$). Copper was used as the substrate material to support the Li layer and heat dissipation, while water was used as the coolant.

Considering that the Gyroid structure has periodic variations in all three directions with identical periodic sizes, the multichannel neutron target station model was simplified to a single-channel neutron target station model to simplify the numerical calculation (the Gyroid structure is simplified from 12 × 12 × 1 units to 4 × 4 × 1 units). Additionally, 40 mm smooth channels were set at the inlet and outlet to reduce inlet and outlet effects, as shown in Fig. 3.

The heating region was located at the bottom surface of the Gyroid structure, with a length of 40 mm and width of 10 mm, using a uniform heat flux density for heating. A proton beam with an energy of 2.8 MeV and a current of 10 mA was used in this study to bombard the Li target, and the proton beam was uniformly distributed, with a circular spot having a radius of 5 cm [29]. During the proton bombardment of the Li target to produce neutrons, more than 99.9 % of the energy is deposited as heat at the neutron target station. Therefore, the heat flux density is set to 3.565 MW/m^2. The inlet and outlet diameters were 6 mm, with an inlet fluid velocity of 3.537 m/s, and a total volumetric flow rate of 0.36 m^3/h.

2.2. Improved Gyroid structure and corresponding mathematical equation

A method for precisely controlling the Gyroid structure is proposed in this study by introducing control factors α into the standard Gyroid function. By adjusting the value of control factor (α), the “through-

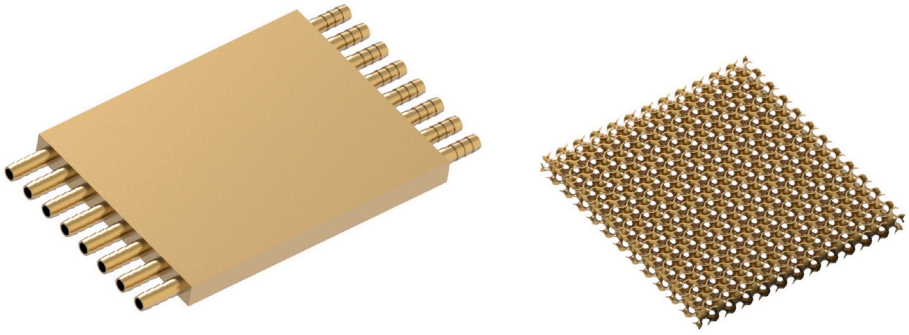

(a) neutron target station substrate

(b) neutron target station internal cooling structure

Fig. 2. BNCT neutron target station model.

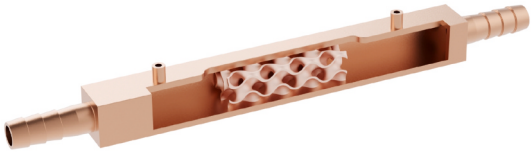

Fig. 3. Single-channel neutron target station model.

holes" in the Gyroid structure can be gradually closed. The mathematical governing equations for the standard Gyroid structure and the improved Gyroid structure are shown in Equations (1) and (2), where L represents the unit length of the TPMS structure, and C denotes the offset of the original unit surface. The control terms $\cos\left(\frac{2\pi}{L}\sin\left(\frac{2\pi}{L}z\right)\cdot\alpha\right)$ is introduced into the standard Gyroid function to form an improved Gyroid function, where α is referred to as the "through-hole" factor. When α is zero, the improved Gyroid function is identical to the standard Gyroid function. The size and shape of the "through-holes" in the Gyroid structure can be adjusted by controlling the value of α. This control term was selected because of its ability to precisely control the Gyroid structure without compromising its inherent topology and connectivity.

Original Gyroid:

$$\cos\left(\frac{2\pi}{L}x\right)\sin\left(\frac{2\pi}{L}y\right)+\cos\left(\frac{2\pi}{L}y\right)\sin\left(\frac{2\pi}{L}z\right)+\cos\left(\frac{2\pi}{L}z\right)\sin\left(\frac{2\pi}{L}x\right)=C \tag{1}$$

Improved Gyroid:

$$\begin{aligned}&\cos\left(\frac{2\pi}{L}x\right)\sin\left(\frac{2\pi}{L}y\right)\cos\left(\frac{2\pi}{L}\sin\left(\frac{2\pi}{L}z\right)\cdot\alpha\right)+\\&\cos\left(\frac{2\pi}{L}y\right)\sin\left(\frac{2\pi}{L}z\right)\cos\left(\frac{2\pi}{L}\sin\left(\frac{2\pi}{L}x\right)\cdot\alpha\right)+\\&\cos\left(\frac{2\pi}{L}z\right)\sin\left(\frac{2\pi}{L}x\right)\cos\left(\frac{2\pi}{L}\sin\left(\frac{2\pi}{L}y\right)\cdot\alpha\right)=C\end{aligned} \tag{2}$$

To maintain the structural characteristics of the standard Gyroid function, after repeated adjustments, the range of values for α was determined as $-2.5 \le \alpha \le 2.5$. The Gyroid unit structures under different values of α are shown in Fig. 4 (with unit length L set to 10 mm, thickness z set to 0.5 mm, and unit surface offset C set to 0). Consequently, by adjusting the "through-hole" factor α, the surface morphology of the Gyroid structure can significantly change. From the frontal view, as the "through-hole" factor α increases, the size and shape of the "through-holes" in the Gyroid structure change significantly, with the "through-holes" gradually transitioning from circular to elliptical, and eventually completely closed when α reaches 2.5.

3. Numerical simulation method and experimental setup

3.1. Governing equation and main evaluation indicators

The governing equations of mass, momentum, and energy are respectively shown as follows:

Mass equation,

$$\nabla\cdot(\rho\vec{v})=0 \tag{3}$$

Momentum equation,

$$\nabla\cdot(\rho\vec{v}\vec{v})=-\nabla p+\nabla\cdot(\bar{\bar{\tau}})+\rho\vec{g}+\vec{F} \tag{4}$$

Where

$$\bar{\bar{\tau}}=\mu\left[(\nabla\vec{v}+\nabla\vec{v}^{T})-\frac{2}{3}\nabla\cdot\vec{v}\cdot\vec{I}\right] \tag{5}$$

Energy equation,

$$\nabla\cdot\left[\rho\vec{v}\left(h+\frac{v^2}{2}\right)\right]=\nabla\cdot\left(k_{eff}\nabla T-\sum_j h_j\vec{J}_j+\bar{\bar{\tau}}_{eff}\cdot\vec{v}\right)+S_h \tag{6}$$

Where, $k_{eff} = k + k_{turb}$, which the turbulence effect enhances the heat transfer effect.

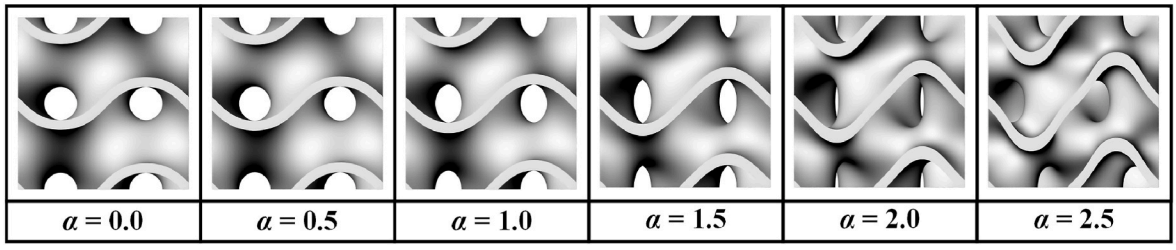

Fig. 4. Impact of different α values on Gyroid structure.

This study consider physical properties and dimensionless numbers, all of which were calculated using Equations (7)–(12).

The Reynolds number is an important parameter that describes the fluid flow. According to this definition, the calculation formula is as follows:

$$Re = \frac{\rho D_h v}{\mu} \tag{7}$$

where ρ represents the fluid density, D_h denotes the hydraulic diameter, v is the inlet velocity, and μ represents the dynamic viscosity.

The calculation method for the hydraulic diameter (D_h) is as follows [30]:

$$D_h = \frac{4V_f}{A_f} \tag{8}$$

where V_f is the volume of the fluid region and A_f is the wetted surface area of the TPMS structure.

The convective heat transfer coefficient describes the heat transfer ability between a fluid and solid interface. The formula is as follows:

$$h = \frac{Q}{T_w - T_f} \tag{9}$$

where Q is the average heat flux density of the heating surface, T_w is the average temperature of heating surface, and T_f is the average temperature of fluid, which is expressed as $T_f = (T_{in} + T_{out})/2$, T_{in} and T_{out} are the inlet and outlet temperatures, respectively.

The Nusselt number is a crucial indicator of the heat transfer capability during the heat transfer process. The calculation method is as follows:

$$Nu = \frac{hD_h}{\lambda} \tag{10}$$

where λ denotes the fluid thermal conductivity.

The friction factor f is a dimensionless parameter introduced in the fluid flow calculations. This can be calculated using the following formula [31]:

$$f = \frac{2\Delta p D_h}{\rho v^2 L_g} \tag{11}$$

where Δp is the pressure drop of the fluid through the Gyroid structure and L_g is the length of the Gyroid structure.

The performance evaluation coefficient (*PEC*) is used to evaluate the overall heat performance, which is defined as [32]:

$$PEC = \frac{Nu_i/Nu_s}{(f_i/f_s)^{1/3}} \tag{12}$$

where subscripts i and s represents the improved and standard Gyroid structures, respectively.

3.2. Grid independency verification

Based on the conclusions of Ref. [33], the *SST k-ω* model yield results much closer to the experimental data than other turbulence model. Therefore, a CFD program was used as the solver in the simulation process, and the *SST k-ω* model and second-order upwind scheme of the discretization of momentum and energy equations were selected. The coupled algorithm was adopted to solve in the pressure-velocity coupling, and the energy residual was set to 10^{-6}.

The number of grids affects both the accuracy of the calculations and convergence time. Therefore, it is necessary to select an appropriate number of grids to improve the computational efficiency and accuracy. In this study, a standard Gyroid structure was chosen to evaluate grid independence, and ten different grid configurations were generated. The temperatures at five representative points on the heating surface (as shown in Fig. 5) were calculated under ten different grid configurations, and the corresponding results are presented in Fig. 6.

It can be observed that as the number of grids gradually increases, the changes in the calculation results gradually diminish. When the number of grids reaches 1,837,532, the variation in the calculation results becomes negligible. Therefore, considering both the computational accuracy and computational time, it was ultimately chosen for subsequent numerical calculations.

3.3. Experimental setup

An experimental approach was employed to validate the accuracy of numerical the simulation results. The experimental system and schematics are shown in Figs. 7 and 8. The experimental setup comprised an AlN heating plate, K-type thermocouples, temperature sensor, flowmeter, differential pressure transmitter, National Instruments (NI) data acquisition system, water pump, and regulating valve. The AlN heating plate, with a power of 500 W and a heat flux density of 125 W/cm^3, provides a stable heat source for the experiment.

The Gyroid experimental model shown in Fig. 9 was fabricated using selective laser melting (SLM) technology with oxygen-free pure copper as the material. After 3D printing, the model underwent heat treatment, resulting in a thermal conductivity of 398 W/(m·K) and a density of 8.92 g/cm^3. To improve the interfacial thermal conductance, an indium-tin alloy was applied between the heating plate and the Gyroid structure, significantly reducing the contact thermal resistance. The indium-tin alloy has a thermal conductivity of 80 W/(m·K), density of 6.89 g/cm^3, and melting point of 333 K.

3.4. Experimental uncertainty analysis

Measurement errors in experimental data can be categorized into direct and indirect errors, which significantly impact the accuracy of results. Direct errors arise from equipment or human influences, while indirect errors are calculated using error transfer formulas. Direct measurement parameters include volume flow rate, pressure, and temperature, while indirect parameters include Reynolds number (*Re*), Nusselt number (*Nu*), friction factor (*f*), heat transfer coefficient (*h*), fluid flow rate (*v*), and heat flow density (*q*). The direct measurement errors and indirect measurement errors are calculated as follows. The uncertainty analysis in this paper refers to the Robert J. Moffat [34].

The formula for calculating the error of the directly measured parameters is as follows:

$$x_i = x_{i,m} \pm \delta x_i \tag{13}$$

where $x_{i,m}$ is the measured value; δx_i is the absolute error of x_i; $\delta x_i/x_i$ is the relative error of x_i.

The formula for calculating the error of indirectly measured parameters is as follows:

$$\delta Y = \sqrt{\sum_i^n \left(\frac{\delta Y}{\delta x_i}\delta x_i\right)^2} \tag{14}$$

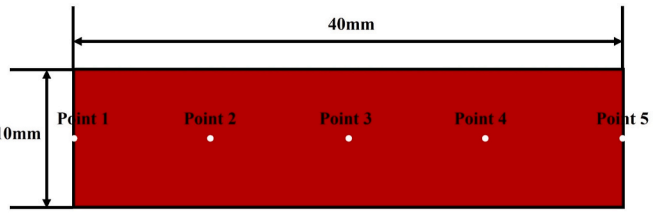

Fig. 5. Five representative points on the heating surface.

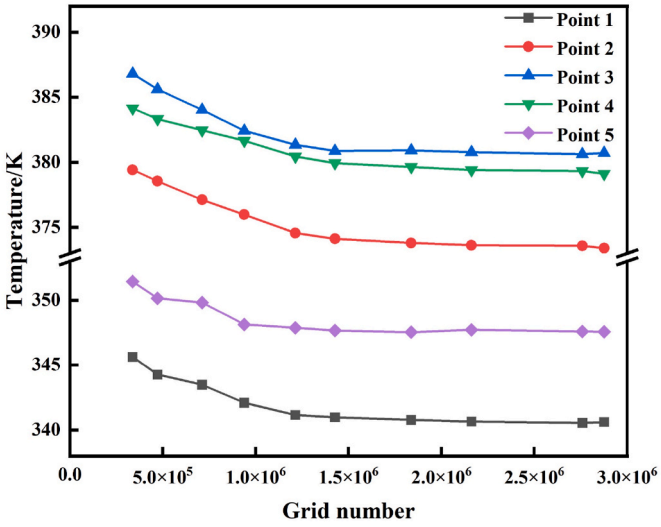

Fig. 6. Verification for grid independence.

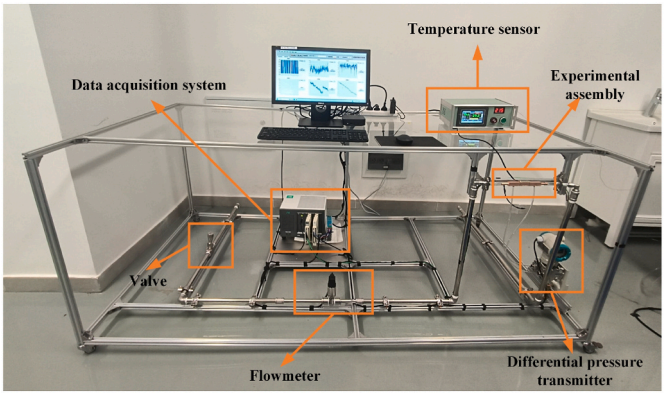

Fig. 7. Picture of experimental system.

Where Y is a function calculated from n independently measured parameters and can be expressed as $Y = f(x_1, x_2, x_3, \cdots x_n)$; δY is the absolute error of the measured value; $\delta Y/Y$ is the relative error of the measured value.

In this experiment, the primary measured parameters include temperature, flow rate, and pressure drop. Temperature measurements were conducted using thermocouples with a range of 253 K–473 K and an accuracy of ±1 %. The flow rate was measured by a flowmeter with a range of 0–1.2 m^3/h and an accuracy of ±1 %. Pressure drop data were obtained using a differential pressure transmitter with a range of 0–500 KPa and an accuracy of ±0.075 %. All experimental data were collected in real-time using the NI data acquisition system. Temperature data were acquired through the NI TB-4353 thermocouple acquisition card with an accuracy of ±0.1 %. Flow rate and pressure drop data were recorded by the NI TB-4300C data acquisition card, also with an accuracy of ±0.1 %.

(1) Maximum relative error of temperature (T): the accuracy of the K-type thermocouple used in the experiment is 1 %, and the minimum temperature in the experimental process is the inlet setup temperature of 293K, so the maximum relative error of the calculated T is:

$$\frac{\Delta T}{T} = \frac{(473 - 253) \times 1\%}{293} \times 100\% = 0.75\% \tag{15}$$

Since the final measurements need to be captured by the data acquisition instrument, the relative error of the final measurements needs to be determined in conjunction with the 0.1 % accuracy of the data acquisition module:

$$\frac{\Delta T}{T} = \sqrt{(0.75\%)^2 + (0.1\%)^2} = 0.76\% \tag{16}$$

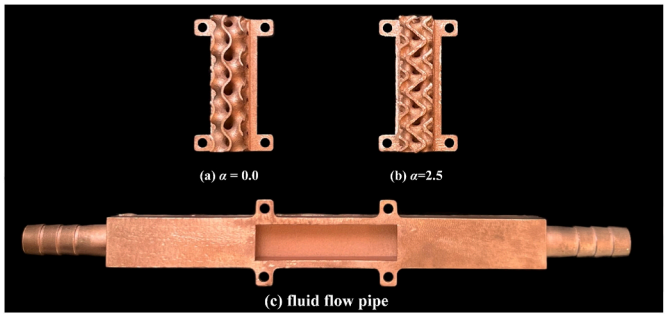

Fig. 9. 3D printed Gyroid structure.

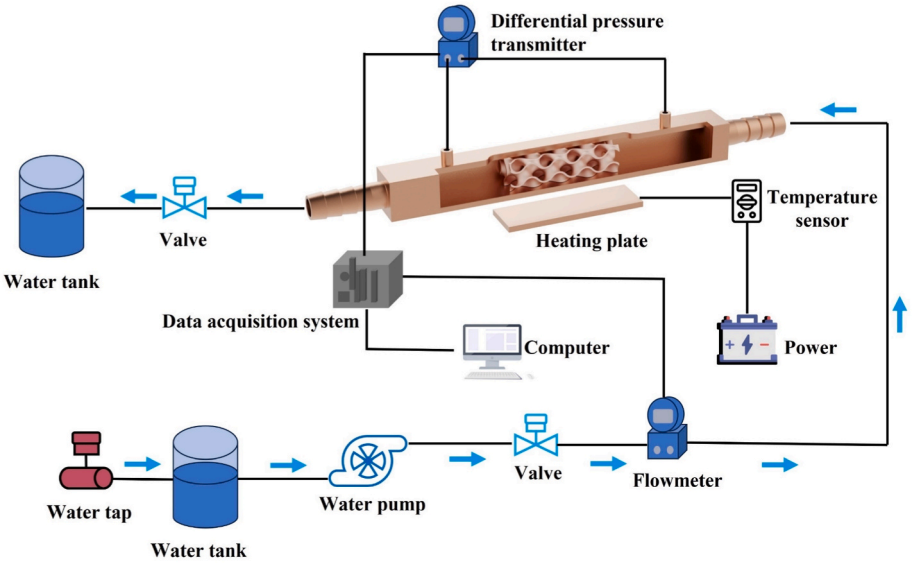

Fig. 8. Schematic of experimental principle.

The calculation results show that the error caused by the data acquisition module is very small, and the effect on the experimental results can be ignored.

(2) Maximum relative error of pressure (P): the accuracy of the pressure sensor used in the experiment is 0.075 %, and the minimum pressure during the experiment is atmospheric pressure (101.325 KPa), the maximum relative error of the calculated P is:

$$\frac{\Delta p}{p}=\sqrt{\left(\frac{(500-0)\times 0.075\%}{101.325}\times 100\%\right)^2+(0.1\%)^2}=0.38\% \tag{17}$$

(3) Maximum relative error of volumetric flow rate (q): the accuracy of the flow meter used in the experiment is 1 %, and the minimum flow rate during the experiment was the inlet set flow rate of 0.12 m^3/h, the maximum error of q is:

$$\frac{\Delta q}{q}=\sqrt{\left(\frac{(1.2-0)\times 1\%}{0.12}\times 100\%\right)^2+(0.1\%)^2}=10.00\% \tag{18}$$

4. Results and discussion

4.1. Comparison of experimental and numerical simulation results

The comparison results between experimental and numerical simulations for Δp and T_{max} across two types of Gyroid structures under different volumetric flow rates are shown in Fig. 10. For $\alpha = 0.0$, which represents the standard Gyroid structure, the maximum deviation of Δp and T_{max} are 4.91 % and 1.20 %, respectively. For $\alpha = 2.5$, which represents the Gyroid structure with completely closed "through-holes", the maximum deviations in Δp and T_{max} are 4.75 % and 0.87 %, respectively. The experimental results and numerical simulations show a high degree of agreement, with deviations in both the Δp and T_{max} within an acceptable range, meeting the error requirements for heat transfer experiments.

The experimental results show that when the "through-holes" in the Gyroid structure are closed, Δp across the Gyroid structure significantly increases, indicating that the resistance of the fluid to flow through the structures increases. Despite the increase in Δp, the T_{max} of the heating surface decreases significantly. Therefore, the closure of "through-holes" in the Gyroid structure causes more complex fluid dynamics, promoting fluid mixing and turbulence, which in turn enhances heat transfer efficiency.

4.2. Impact of α on flow characteristics

The velocity distribution contours and streamlines at the $x = 0$, $y = 0$, and $z = 0$ cross-sections for different α values are shown in Figs. 11–13, respectively. It can be observed that increasing the value of α has a significant effect on the distribution of velocity field. When $\alpha = 0.0$, the fluid velocity distribution in the Gyroid structure is relatively uniform, and the high-velocity regions are concentrated in the center of the channel, while velocity near the wall is low. However, as the value of α increases, the velocity distribution gradually becomes non-uniform. When α increases to 2.5, a noticeable alternation of high and low velocity regions can be observed, indicating that the fluid flow is subjected to larger-scale disturbances. The drastic changes in velocity indicate that the nonlinearity of the fluid flow was enhanced, and the fluid experienced more intensive mixing and turbulence effects within the channels.

Furthermore, the vortex structures in the streamlines changed significantly as α increased. When $\alpha = 0.0$, the streamlines are relatively orderly, with fewer vortex structures, and the flow remains steady. However, as the value of α increases, the streamlines become more complex, with numerous small-scale vortices and localized turbulent phenomena. These vortices significantly enhance the mixing effect of the fluid within the channels. When $\alpha = 2.5$, intensely turbulent flow phenomena can be observed across various cross-sections, with streamlines twisting, intersecting, and forming multiple small vortex regions. Under these conditions, the fluid exhibits a high degree of instability, indicating that as the value of α increases, the flow within the Gyroid structure gradually changes from an orderly state to a disordered turbulent state. This is because with the increase of α, the "through holes" in the Gyroid structure are gradually closed, forcing the fluid into the non-linear flow path formed by the complex surface of the Gyroid, which disrupts the boundary layer and generates more secondary flows and vortices, thereby improving the convective heat transfer performance.

Enhanced convective heat transfer is often accompanied by an increase in pressure drop and flow resistance. The impact of varying α on the pressure drop (Δp) and f in the Gyroid structure is illustrated in Fig. 14. With an increase in volumetric flow rate, Δp in the Gyroid structure increases exponentially. This is because, as the volumetric flow rate increases, the inertial forces of the fluid are gradually becoming dominant. When the volumetric flow rate is within the range of 0.12–0.72 m^3/h, Δp in the improved Gyroid structure gradually increases as α increases. In the lower range of α values (0–1.5), the increase in Δp is relatively slow. However, when α reaches 2.0 and 2.5, Δp is significantly increased, rising by 33.8–36.9 % and 266.5–272.6 %, respectively, compared to the standard Gyroid structure.

With the value of α increases, f initially decreases and then increases,

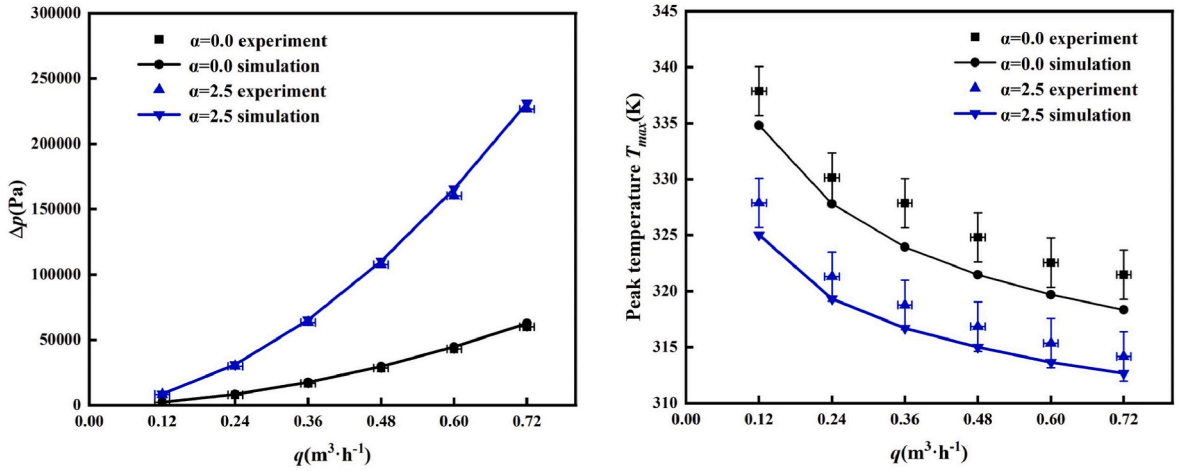

Fig. 10. Comparison of the experimental and numerical simulation results.

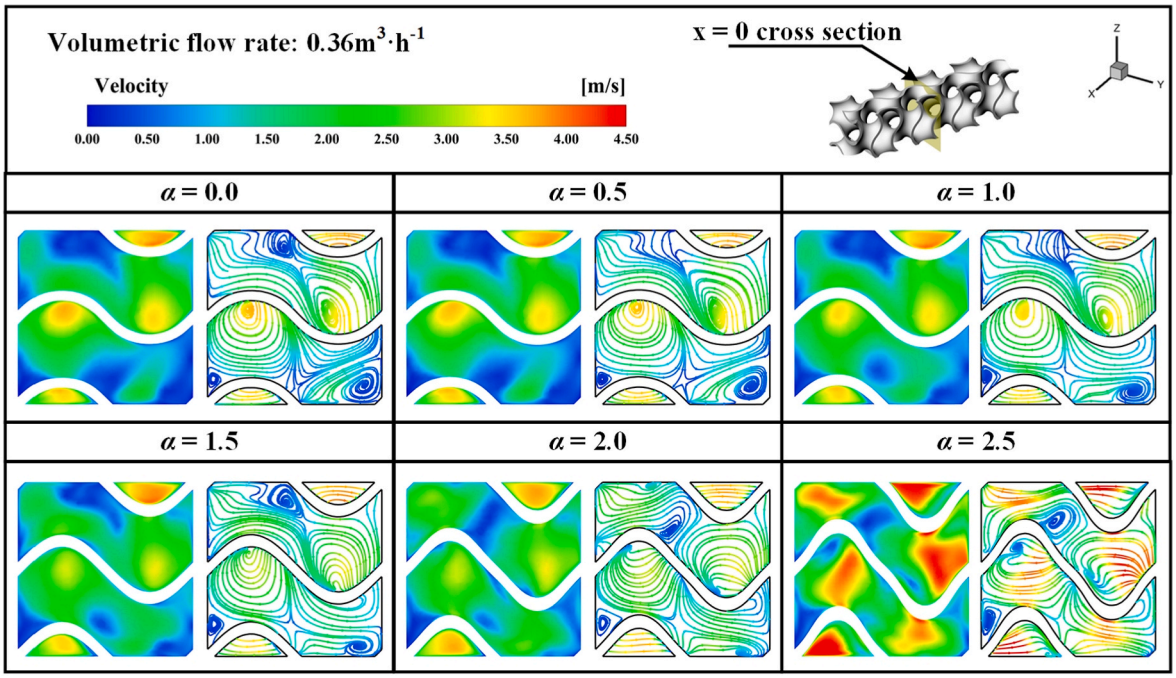

Fig. 11. Velocity distribution contours and streamlines at the $x = 0$ cross-section for different α values.

reaching a minimum at $\alpha = 1.5$. This phenomenon can be explained by the relatively slow increase in Δp within the lower range of α values (0.5–1.5), and the closure of "through-holes" in the Gyroid structure, which disrupts the fluid boundary layer, reduces the relative influence of viscous forces, and ultimately causes a decrease in f. This trend typically reflects an enhancement in the turbulent effects within the flow. Moreover, f in the Gyroid structure gradually decreased with increasing Re. This was because, as Re increased, the inertial forces of the fluid became dominant, whereas the relative influence of the viscous forces diminished, thereby reducing f.

4.3. Impact of α on heat transfer characteristics

The temperature distribution contours at the $x = 0$, $y = 0$, and $z = 0$ cross-sections for different α values are shown in Figs. 15–17, respectively. When $\alpha = 0.0$, the temperature field of the Gyroid structure exhibits significant laminar characteristics, and the temperature gradient is concentrated near the heating surface, with a relatively smooth and orderly distribution. This is owing to the weak mixing of the fluid, which causes a relatively low heat transfer efficiency from the heating surface to the fluid interior, resulting in a temperature gradient typically concentrated near the heating surface, whereas the temperature at the center of the flow channel remains relatively low, thus limiting the heat transfer efficiency. As α increases, the "through-holes" in the Gyroid structure are gradually closed, and complex flow paths and vortex generation cause a more chaotic flow field, which effectively promotes the mixing and redistribution of fluid, resulting in more uniform heat dispersion throughout the Gyroid structure. High-temperature regions are not confined to the vicinity of the heating surface, and heat is diffused to the center of the flow channel through fluid convection. Consequently, the mixing effect of the fluid and convective heat transfer were significantly enhanced.

The temperature distribution contours at the heating surface for different α values are shown in Fig. 18. It can be observed that increasing the value of α has a significant impact on the distribution of the temperature field on the heating surface. When $\alpha = 0.0$, the temperature field on the heating surface of the Gyroid structure is significantly non-uniform, with a noticeable temperature gradient, reaching a peak temperature 381.2 K. As α increases, the peak temperature on the heating surface of the Gyroid structure gradually decreases, and the temperature distribution becomes more uniform. When α increases to 2.5, the peak temperature of the Gyroid structure drops to 360.6 K, indicating that the fluid mixing effects and convective heat transfer were significantly enhanced, resulting in a more uniform heat distribution on the heating surface. Compared with the standard Gyroid structure, the Gyroid structure with closed "through-holes" exhibits significant advantages in terms of thermal management, effectively reducing local temperatures and improving the uniformity of the temperature distribution, thereby enhancing the heat transfer performance.

The impact of α on T_{max} and h of the heating surface of the Gyroid structure are shown in Fig. 19. As the volumetric flow rate increased, T_{max} of the Gyroid structure exhibited a linear decreasing trend, while h showed a linear increasing trend. Within the volumetric flow rate range of 0.12–0.72 m^3/h, as the value of α increases, T_{max} of the improved Gyroid structure gradually decreases, and h gradually increases. When α increases to 2.5, T_{max} of the Gyroid structure decreases by 16.1–27.9 K, while h increases by 28.3–33.0 %.

The impact of α on the Nu of the Gyroid structure is illustrated in Fig. 20. As Re increases, the Nu of the Gyroid structure also exhibited a linearly increasing trend. However, unlike h, the Nu of the modified Gyroid structure first increases and then decreases as α increases, reaching its maximum value at $\alpha = 1.5$. Compared to the standard Gyroid structure, Nu of the improved Gyroid structure increases by 1.4–3.2 %.

In addition, the relationship between Nu and Re for the standard Gyroid structure ($\alpha = 0.0$) and the Gyroid structure with completely closed "through-holes" ($\alpha = 2.5$) was fitted in this study, and the corresponding empirical formulas were derived.

For the standard Gyroid structure ($\alpha = 0.0$), the fitted empirical formulas between Nu and Re is expressed by:

$$Nu = 30.11Re^{0.270} \tag{19}$$

For the Gyroid structure with completely closed "through-holes" ($\alpha = 2.5$), the fitted empirical formulas between Nu and Re is denoted by:

$$Nu = 34.56Re^{0.247} \tag{20}$$

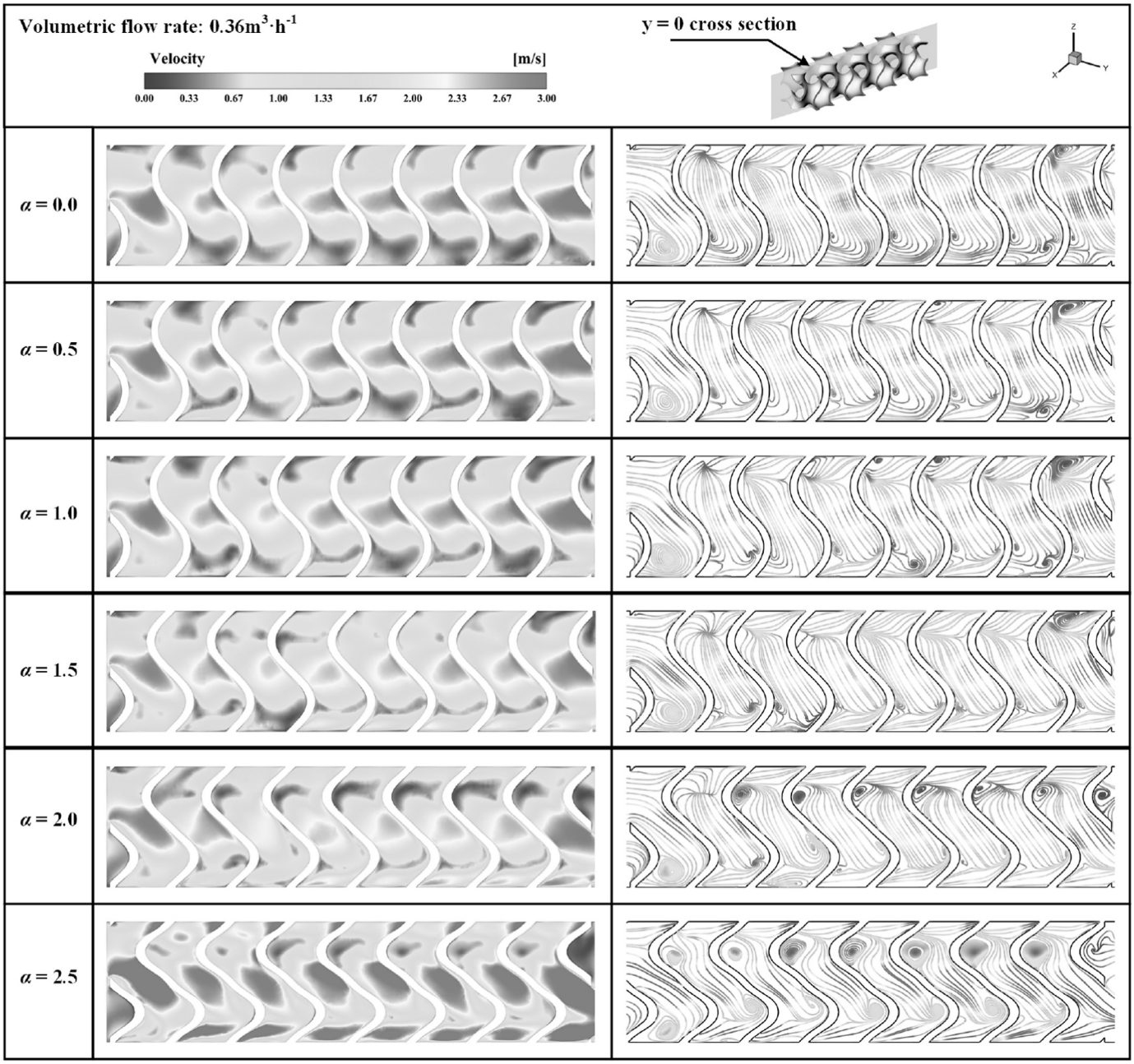

Fig. 12. Velocity distribution contours and streamlines at the $y = 0$ cross-section for different α values.

It should be noted that Equations (19) and (20) are derived based on numerical simulation results within the Reynolds number range of 1000–9000. Therefore, these correlations are valid only within this specified range. Their applicability outside of this range may be limited, and care should be taken when extending their use beyond the studied range. Within the defined range, however, these formulas provide a valuable reference for evaluating and optimizing the thermal performance of Gyroid-based heat transfer structures.

4.4. Overall evaluation of heat transfer performance

By adjusting the α parameters of the Gyroid structure, the design can be optimized to achieve optimal heat transfer performance under specific fluid conditions. When an overall enhancement in heat transfer efficiency is required, increasing the α value can be effective. Conversely, to balance heat transfer performance and pressure drop, moderate α values should be selected to achieve optimal results. The improved Gyroid structure achieves better convective heat transfer performance compared to the standard Gyroid structure, however, with increasing volumetric flow rate, the pressure drop (Δp) of the Gyroid structure grows exponentially, which is unfavorable for practical applications. Therefore, it becomes particularly important to discuss the comprehensive heat transfer performance of the Gyroid structure.

The performance evaluation factor (PEC) used in this paper is calculated based on the standard Gyroid structure, where PEC >1 indicates that the overall performance of the improved Gyroid structure, considering both heat transfer and flow resistance, is superior to that of the standard Gyroid structure. The influence of α on the *PEC* of the Gyroid structure is illustrated in Fig. 21. As α increases, the *PEC* of the improved Gyroid structure initially rises, reaching a peak at $\alpha = 1.5$, and then declines. Although the improved Gyroid structure exhibits the highest convective heat transfer coefficient and the lowest peak

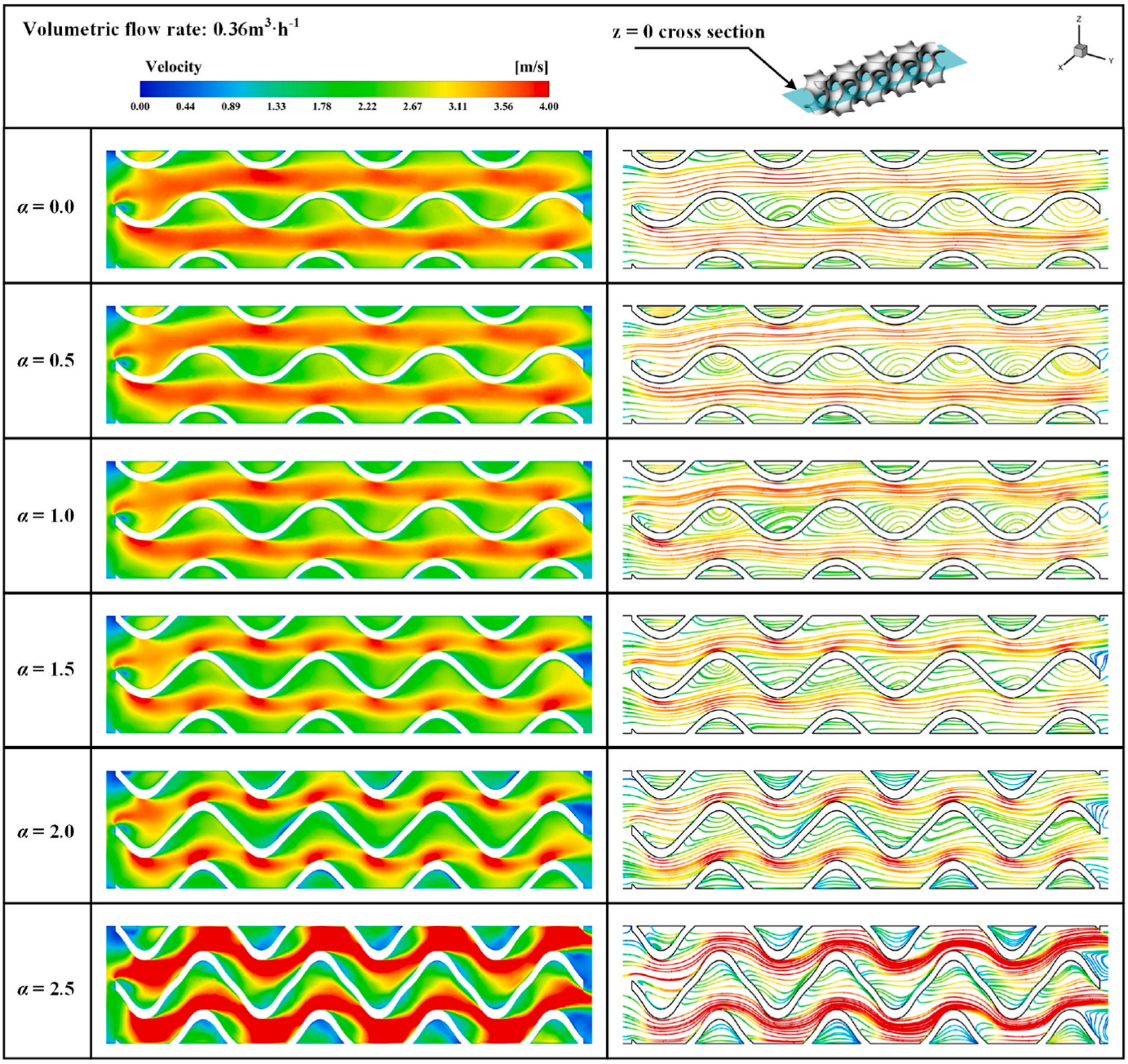

Fig. 13. Velocity distribution contours and streamlines at the $z = 0$ cross-section for different α values.

temperature at $\alpha = 2.5$, the *PEC* value falls below 1, indicating that its overall performance is inferior to the standard Gyroid structure. According to the definition and physical meanings of *PEC*, the *PEC* value reflects the overall efficiency considering both heat transfer and flow resistance. Any case where *PEC* is greater than 1 is desirable. Here, it is suggested that the α value of 2.0 is more appropriate, because the flow pressure drop is large when the α value is 2.5, and the heat transfer is not strong enough when the α value is 1.5. Additionally, the improved Gyroid structure possesses a relatively high convective heat transfer coefficient and a lower peak temperature.

In practical applications, although the convective heat transfer performance of the Gyroid structure is significantly improved under the condition of $\alpha = 2.5$, it is important to note that this improvement comes at the cost of increased flow resistance. This implies that in the design and optimization of heat exchange systems, a trade-off must be made between heat transfer efficiency and flow resistance. If the priority is to enhance heat transfer efficiency and the system can tolerate a higher pressure drop, then the configuration of $\alpha = 2.5$ might be an appropriate choice. However, if flow resistance is a critical limiting factor, it may be necessary to compromise under other conditions to achieve a more balanced performance. The final choice should be based on the specific application requirements and constraints, taking into account both heat transfer performance and system energy consumption.

In the BNCT neutron target cooling structure design discussed in this paper, after weighing heat transfer efficiency against flow resistance, the configuration of $\alpha = 2.0$ is a suitable choice for the Gyroid structure of neutron target station. This research provides theoretical guidance for the application of the Gyroid structure in the BNCT neutron target station design, contributing to an efficient and economical heat exchange solution.

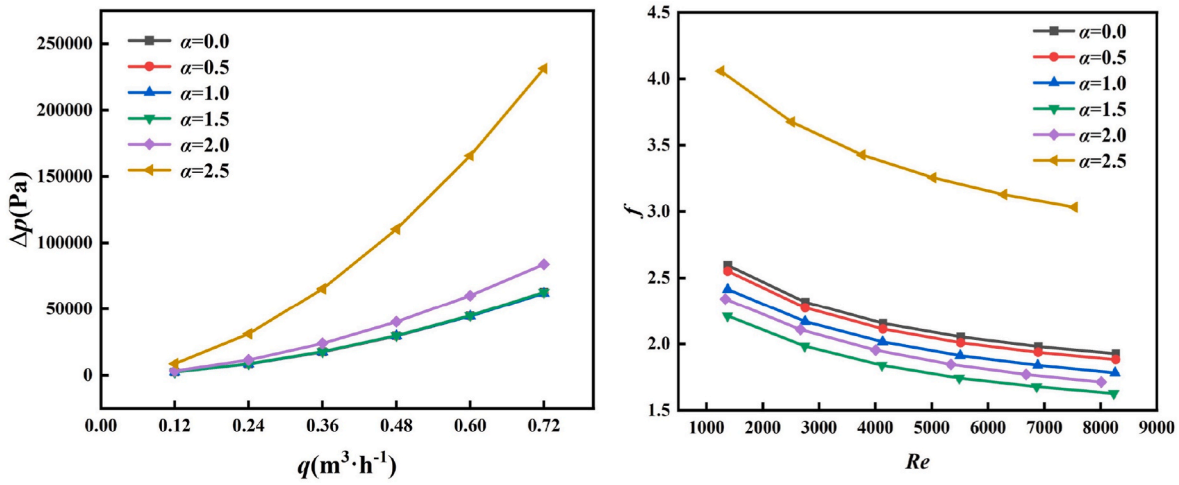

Fig. 14. Impact of α on Δp and f of Gyroid structure.

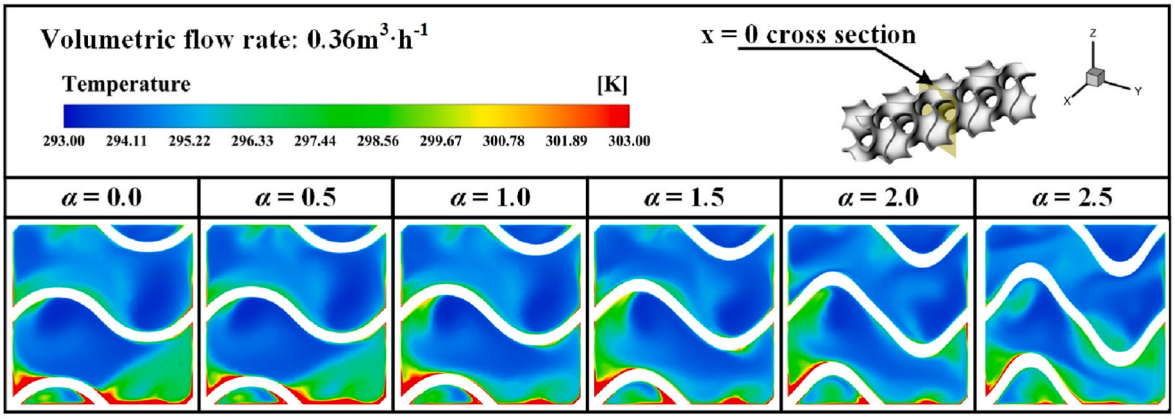

Fig. 15. Temperature distribution contours at the $x = 0$ cross-section for different α values.

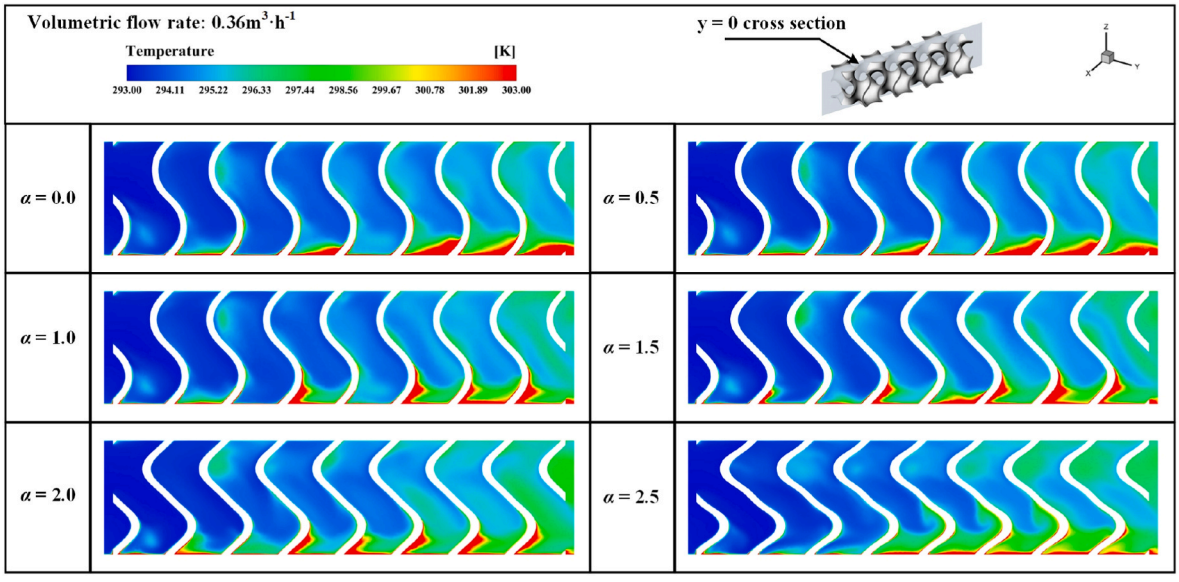

Fig. 16. Temperature distribution contours at the $y = 0$ cross-section for different α values.

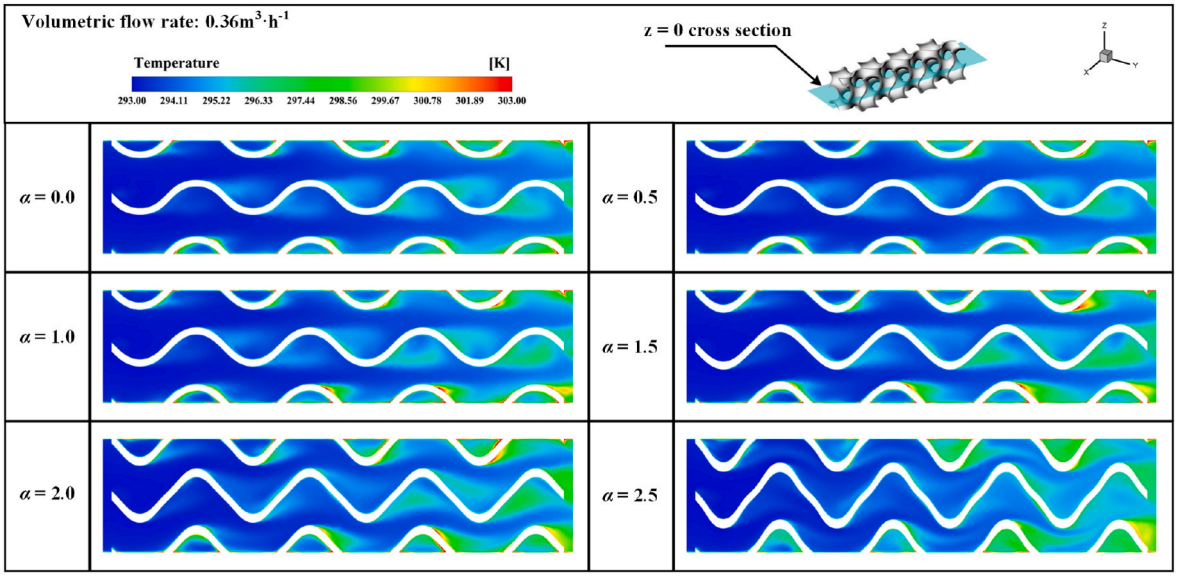

Fig. 17. Temperature distribution contours at the $z = 0$ cross-section for different α values.

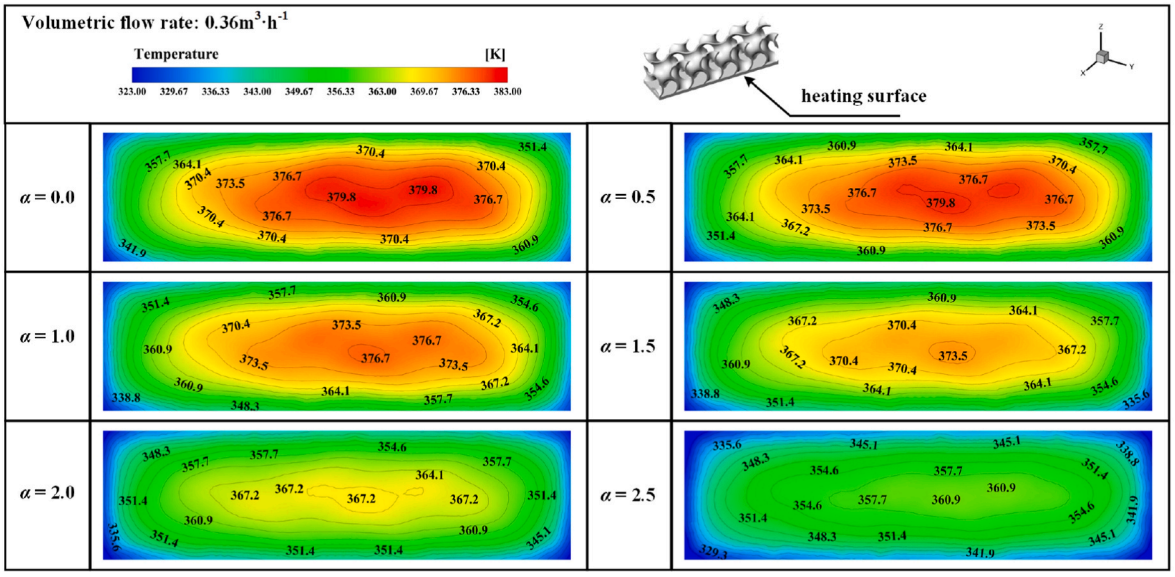

Fig. 18. Temperature distribution contours at heating surface for different α values.

5. Conclusion

To improve the heat removal capability of the BNCT neutron target stations, a method for precisely controlling the Gyroid structure was proposed in this study by introducing control factors α into the standard Gyroid function. The following main conclusions were drawn.

(1) As the value of α increases, T_{max} of the Gyroid structure decreases by 16.1–27.9 K, h increases by 28.3–33 %, and Nu increases by 1.4–3.2 %. The closure of "through-holes" in the Gyroid structure forces the fluid into the non-linear flow path formed by the complex surface of the Gyroid, thereby enhancing the disruption of the boundary layer and generating more secondary flows and vortices.

(2) The relationship between Nu and Re for different types of Gyroid structures was fitted, and the corresponding empirical expressions were derived. The results indicated a significant correlation between Nu and Re within the studied parameter range. The empirical relationship accurately describes the convective heat transfer characteristics and demonstrates high fitting precision.

(3) Enhanced convective heat transfer typically causes increased pressure drop and greater flow resistance. After considering the

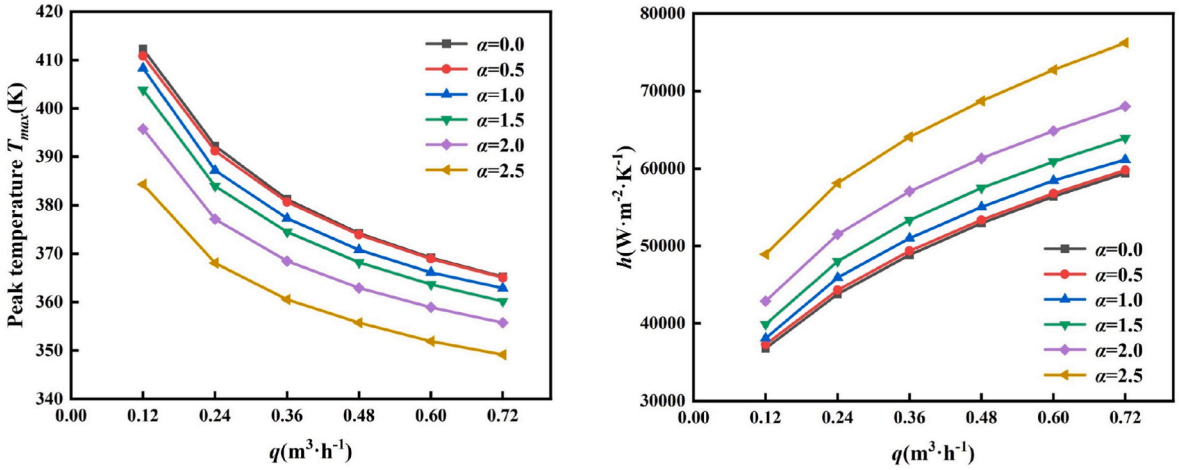

Fig. 19. Impact of α on T_{max} and h of Gyroid structure.

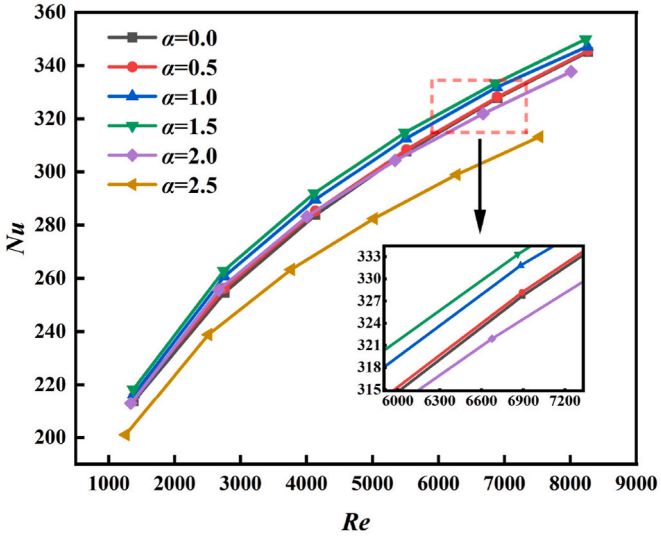

Fig. 20. Impact of α on *Nu* of Gyroid structure.

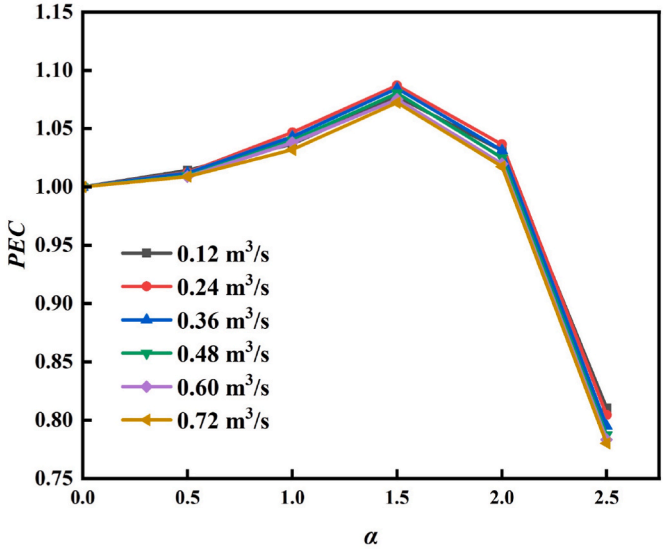

Fig. 21. Impact of α on *PEC* of Gyroid structure.

combined impact of heat transfer efficiency and pressure drop, it is advisable to choose $\alpha = 2.0$ to achieve the best results.

CRediT authorship contribution statement

Kaiwen Qin: Writing – review & editing, Writing – original draft, Funding acquisition, Formal analysis, Data curation, Conceptualization. **Nailiang Zhuang:** Writing – review & editing, Validation, Methodology, Funding acquisition. **Chong Shao:** Writing – review & editing, Software, Formal analysis, Data curation. **Hangbin Zhao:** Writing – review & editing, Software, Methodology, Formal analysis. **Xiaobin Tang:** Writing – review & editing, Software, Methodology, Funding acquisition.

Declaration of competing interest

The authors declare that they have no known competing financial interests or personal relationships that could have appeared to influence the work reported in this paper.

Acknowledgments

This work was supported by the Graduate Research Innovation Program Project of Jiangsu Province (Grant No. KYCX24_0617).

Data availability

Data will be made available on request.

References

[1] M.A. Dymova, S.Y. Taskaev, V.A. Richter, et al., Boron neutron capture therapy: current status and future perspectives, Cancer Commun. 40 (9) (2020) 406–421.
[2] H. He, J. Li, P. Jiang, et al., The basis and advances in clinical application of boron neutron capture therapy, Radiat. Oncol. 16 (2021) 1–8.
[3] S. Wang, Z. Zhang, L. Miao, et al., Boron neutron capture therapy: current status and challenges, Front. Oncol. 12 (2022) 788770.
[4] X. Wang, D. Shu, C. Geng, et al., Advancing 2D reaction rate measurements in BNCT: Validation of the indirect neutron radiography method, Radiat. Meas. 174 (2024) 107133.
[5] P.Y. Lee, X. Tang, C. Geng, et al., A bi-tapered and air-gapped beam shaping assembly used for AB-BNCT, Appl. Radiat. Isot. 167 (2021) 109392.
[6] D.M. Minsky, A.J. Kreiner, Near threshold 7Li (p,n) 7Be reaction as neutron source for BNCT, Appl. Radiat. Isot. 106 (2015) 68–71.
[7] S. Taskaev, E. Berendeev, M. Bikchurina, et al., Neutron source based on vacuum insulated tandem accelerator and lithium target, Biology 10 (5) (2021) 350.
[8] X. Li, Y. Ikeda, T. Kobayashi, et al., Study on the edge-cooling target structure for transportable accelerator-driven neutron source, Nucl. Instrum. Methods Phys. Res. Sect. A Accel. Spectrom. Detect. Assoc. Equip. 1017 (2021) 165793.

[9] S. Park, S.H. Jung, C.Y. Han, et al., A study on thermal optimization of lithium target design for accelerator-based bnct[C], in: Proceedings of the Korean Nuclear Society Conference, Korean Nuclear Society, 2005, pp. 883–884.
[10] S. Yoshihashi, T. Tsuneyoshi, K. Tsuchida, et al., High heat removal technique for a lithium neutron generation target used for an accelerator-driven BNCT system, J. Instrum. 16 (4) (2021) P04016.
[11] S. Nakamura, H. Igaki, H. Okamoto, et al., Dependence of neutrons generated by 7Li (p,n) reaction on Li thickness under free-air condition in accelerator-based boron neutron capture therapy system employing solid-state Li target, Phys. Med. 58 (2019) 121–130.
[12] K. Sato, A. Uritani, K. Watanabe, et al., Improved design of the exit of a beam shaping assembly for an accelerator-driven BNCT system in Nagoya University[C], in: Proceedings of the International Conference on Neutron Optics (NOP2017), 2018 011003.
[13] Y.Q. Wang, J.L. Du, H. Lin, et al., An AB-BNCT epithermal neutron source using 7Li (p,n) 7Be reaction, J. Instrum. 18 (3) (2023) P03006.
[14] B.A. Ludewigt, W.T. Chu, R.J. Donahue, An epithermal neutron source for BNCT based on an ESQ-accelerator, in: The Embedded Topic Meeting on Accelerator Applications, 1997.
[15] S. Nakamura, H. Igaki, M. Ito, et al., Characterization of the relationship between neutron production and thermal load on a target material in an accelerator-based boron neutron capture therapy system employing a solid-state Li target, PLoS One 14 (11) (2019) e0225587.
[16] Y. Hu, X. Li, Y. Lv, et al., Simulations on the thermal and mechanical performance of the rotating target system of accelerator-driven neutron source for Boron Neutron Capture Therapy (BNCT), Nucl. Instrum. Methods Phys. Res. Sect. A Accel. Spectrom. Detect. Assoc. Equip. 1053 (2023) 168340.
[17] J.Y. Wang, H.Y. Kong, D.M. Li, Design of a neutron target for boron neutron capture therapy, Nucl. Tech. 47 (4) (2024) 253–3219 (in chinese).
[18] I. Kaur, P. Singh, Flow and thermal transport characteristics of Triply-Periodic Minimal Surface (TPMS)-based gyroid and Schwarz-P cellular materials, Numer. Heat Transf. A Appl. 79 (8) (2021) 553–569.
[19] K. Dutkowski, M. Kruzel, K. Rokosz, Review of the state-of-the-art uses of minimal surfaces in heat transfer, Energies 15 (21) (2022) 7994.
[20] K. Yeranee, Y. Rao, A review of recent investigations on flow and heat transfer enhancement in cooling channels embedded with triply periodic minimal surfaces (TPMS), Energies 15 (23) (2022) 8994.
[21] W. Rossman, Infinite periodic discrete minimal surfaces without self-intersections, Balkan J. Geometry Its Appl. 10 (2) (2025) 106–128.
[22] D. Cvijović, J. Klinowski, The T and CLP families of triply periodic minimal surfaces. Part 1. Derivation of parametric equations, J. Phys. 2 (2) (1992) 137–147.
[23] J. Feng, J. Fu, C. Shang, et al., Porous scaffold design by solid T-splines and triply periodic minimal surfaces, Comput. Methods Appl. Mech. Eng. 336 (2018) 333–352.
[24] M. Khalil, M.I.H. Ali, K.A. Khan, et al., Forced convection heat transfer in heat sinks with topologies based on triply periodic minimal surfaces, Case Stud. Therm. Eng. 38 (2022) 102313.
[25] T. Dixit, E. Al-Hajri, M.C. Paul, et al., High performance, microarchitected, compact heat exchanger enabled by 3D printing, Appl. Therm. Eng. 210 (2022) 118339.
[26] W. Li, G. Yu, Z. Yu, Bioinspired heat exchangers based on triply periodic minimal surfaces for supercritical CO2 cycles, Appl. Therm. Eng. 179 (2020) 115686.
[27] J. Wang, K. Chen, M. Zeng, et al., Investigation on flow and heat transfer in various channels based on triply periodic minimal surfaces (TPMS), Energy Convers. Manag. 283 (2023) 116955.
[28] W. Tang, H. Zhou, Y. Zeng, et al., Analysis on the convective heat transfer process and performance evaluation of triply periodic minimal surface (TPMS) based on Diamond, gyroid and Iwp, Int. J. Heat Mass Tran. 201 (2023) 123642.
[29] Y. Zhu, Z. Lin, H. Yu, et al., Conceptional design of an adjustable moderator for BNCT based on a neutron source of 2.8 áMeV proton bombarding with Li target, Nucl. Eng. Technol. 56 (5) (2024) 1813–1821.
[30] J. Iyer, T. Moore, D. Nguyen, et al., Heat transfer and pressure drop characteristics of heat exchangers based on triply periodic minimal and periodic nodal surfaces, Appl. Therm. Eng. 209 (2022) 118192.
[31] T. Zhang, F. Liu, K. Zhang, et al., Numerical study on the anisotropy in thermo-fluid behavior of triply periodic minimal surfaces (TPMS), Int. J. Heat Mass Tran. 215 (2023) 124541.
[32] W.S. Huang, H.Y. Ning, N. Li, et al., Thermal-hydraulic performance of TPMS-based regenerators in combined cycle aero-engine, Appl. Therm. Eng. 250 (2024) 123510.
[33] K. Kus, M. Wójcik, Z. Malecha, et al., Numerical and experimental investigation of the gyroid heat exchanger, Int. J. Heat Mass Tran. 231 (2024) 125882.
[34] R.J. Moffat, Describing the uncertainties in experimental results, Exp. Therm. Fluid Sci. 1 (1) (1988) 3–17.